AGU PUBLICATIONS

JGR

Journal of Geophysical Research: Space Physics

RESEARCH ARTICLE

10.1002/2014JA020777

Special Section:
New perspectives on Earth's radiation belt regions from the prime mission of the Van Allen Probes

Upper limit on the inner radiation belt MeV electron intensity

X. Li[1,2], R. S. Selesnick[3], D. N. Baker[1], A. N. Jaynes[1], S. G. Kanekal[4], Q. Schiller[1,2], L. Blum[1,2,5], J. Fennell[6], and J. B. Blake[6]

[1]Laboratory for Atmospheric and Space Physics, University of Colorado Boulder, Boulder, Colorado, USA, [2]Department of Aerospace Engineering Sciences, University of Colorado Boulder, Boulder, Colorado, USA, [3]Space Vehicles Directorate, Air Force Research Laboratory, Kirtland AFB, New Mexico, USA, [4]NASA/Goddard Space Flight Center, Greenbelt, Maryland, USA, [5]Now at Space Sciences Laboratory, University of California, Berkeley, California, USA, [6]Space Science Applications Laboratory, Aerospace Corporation, El Segundo, California, USA

Key Points:
- Quantified upper limit of MeV electrons in the inner belt
- Actual MeV electron intensity likely much lower than the upper limit
- More detailed understanding of relativistic electrons in the magnetosphere

Correspondence to:
X. Li,
lix@lasp.colorado.edu

Citation:
Li, X., R. S. Selesnick, D. N. Baker, A. N. Jaynes, S. G. Kanekal, Q. Schiller, L. Blum, J. Fennell, and J. B. Blake (2015), Upper limit on the inner radiation belt MeV electron intensity, *J. Geophys. Res. Space Physics*, *120*, 1215–1228, doi:10.1002/2014JA020777.

Received 29 OCT 2014
Accepted 14 JAN 2015
Accepted article online 18 JAN 2015
Published online 24 FEB 2015

Abstract No instruments in the inner radiation belt are immune from the unforgiving penetration of the highly energetic protons (tens of MeV to GeV). The inner belt proton flux level, however, is relatively stable; thus, for any given instrument, the proton contamination often leads to a certain background noise. Measurements from the Relativistic Electron and Proton Telescope integrated little experiment on board Colorado Student Space Weather Experiment CubeSat, in a low Earth orbit, clearly demonstrate that there exist sub-MeV electrons in the inner belt because their flux level is orders of magnitude higher than the background, while higher-energy electron (>1.6 MeV) measurements cannot be distinguished from the background. Detailed analysis of high-quality measurements from the Relativistic Electron and Proton Telescope on board Van Allen Probes, in a geo-transfer-like orbit, provides, for the first time, quantified upper limits on MeV electron fluxes in various energy ranges in the inner belt. These upper limits are rather different from flux levels in the AE8 and AE9 models, which were developed based on older data sources. For 1.7, 2.5, and 3.3 MeV electrons, the upper limits are about 1 order of magnitude lower than predicted model fluxes. The implication of this difference is profound in that unless there are extreme solar wind conditions, which have not happened yet since the launch of Van Allen Probes, significant enhancements of MeV electrons do not occur in the inner belt even though such enhancements are commonly seen in the outer belt.

1. Introduction

Earth's radiation belts are divided into three regions: the inner belt, centered near 1.5 Earth radii (R_E) from the center of the Earth when measured in the equatorial plane; the outer belt, which is most intense between 4 and 5 R_E for relativistic electrons (>500 keV); and the "slot" region, centered near 2.5 R_E, which appears to separate the two radiation belts during quiet times but can be filled with relativistic electrons during active times. The outer belt electrons are constantly decaying and episodically reforming, on a time scale of hours to days, and each reformed belt may have a different center location and intensity [*Li and Temerin*, 2001]. In contrast, Earth's inner radiation belt is much more stable. It contains an intense and stable population of geomagnetically trapped protons with kinetic energies up to ~1 GeV, formed by cosmic ray albedo neutron decay (CRAND) and solar proton trapping [*Selesnick et al.*, 2014]. The CRAND process also produces electrons, with kinetic energies primarily below 800 keV but is thought not to be a significant source of trapped electrons [*Lenchek et al.*, 1961]. This conclusion is supported by the unsteady nature of inner belt electron intensity observed at these lower energies, with rapid (~1 day) injections followed by slow decay [*Rosen and Sanders*, 1971]. Exponential decay timescales (*e*-folding times) are ~100 days [*Selesnick*, 2012]. Injections occur most frequently at the lower energies (<600 keV), typically several times per year [*Zhao and Li*, 2013b], but only occasionally for higher kinetic energies, $E \geq$ ~1 MeV [*Baker et al.*, 2007; *Zhao and Li*, 2013a]. Intense high-energy injections occurred in March 1991 [*Blake et al.*, 1992], associated with an unusually strong interplanetary shock [*Li et al.*, 1993], and October 2003 [*Baker et al.*, 2004], that produced an extreme magnetic storm ($Dst \lesssim -400$ nT) and for which the injection mechanisms are still debated [*Horne et al.*, 2005; *Kress et al.*, 2007; *Li et al.*, 2009]. The trapped multiple-MeV electrons with decaying intensity were subsequently observed for years in each case [e.g., *Looper et al.*, 1994].

Rare injections of high-energy electrons into the inner belt undoubtedly occur. However, some measurements, which are subject to contamination from inner belt protons, might have suggested a steady

population of high-energy inner-belt-trapped electrons. The relative stability of the inner belt has been attributed to continuous replenishment by inward diffusion of electrons from the outer radiation belt [*Lyons and Thorne*, 1973]. Although the viability of such a source has been questioned [*Kim and Shprits*, 2012], the reality of a stable-trapped electron population typically has not. In fact, the widely applied AE8 and AE9 empirical radiation belt models both specify substantial populations of inner belt high-energy electrons without any time dependence [*Vette*, 1991; *Ginet et al.*, 2013].

A strong resemblance between the stable inner belt proton distribution and the supposed electron distribution, in both space and time, is a clue that they may, in fact, be one and the same. The reliability of proton measurements is well documented [*Selesnick et al.*, 2014] but not so for MeV electrons. Therefore, the possibility should be carefully considered that other measurements of a stable inner belt electron intensity for $E \geq \sim 1$ MeV are erroneous, resulting from contamination by protons.

In this paper, data from the Relativistic Electron Proton Telescope (REPT) [*Baker et al.*, 2012] on each of the two Van Allen Probes satellites [*Mauk et al.*, 2012; *Kessel et al.*, 2012] and the Relativistic Electron Proton Telescope integrated little experiment (REPTile) on board Colorado Student Space Weather Experiment (CSSWE) [*Li et al.*, 2012, 2013a] are analyzed for possible detection of inner belt high-energy electrons. REPT is part of the Radiation Belt Storm Probes-Energetic Particle, Composition, and Thermal Plasma (RBSP-ECT) suite [*Spence et al.*, 2013], which consists of three sets of measurements: Helium, Oxygen, Proton, and Electron (HOPE) [*Funstein et al.*, 2013] covering 10 eV to 50 keV; Magnetic Electron Ion Spectrometer (MagEIS) [*Blake et al.*, 2013] covering 37 keV to 4 MeV; and REPT covering 1.6 MeV to 10 MeV electrons with each sensor designed to reduce or remove backgrounds expected from protons in the inner zone.

2. REPT and REPTile Data

REPT contains a stack of nine aligned Si solid state detectors that each measures energy deposition from charged particles. In combination they provide an accurate determination of incident kinetic energy for particles that enter through the front collimator (with a 32° field of view) and stop in one of the detectors and integral energy determinations for those particles that fully penetrate the stack. Discrimination between species and energy of protons and electrons is nominally achieved from a set of logic conditions [*Baker et al.*, 2012]. However, for the analysis presented in the paper, the logic conditions are not used but replaced by equation (1) to be described in section 3.

A subset of the REPT data are available as pulse height analyzer (PHA) events with fast time resolution (12 ms between events) that specify the energy deposits measured simultaneously in every detector. Each event ideally represents a single charged particle measurement. Together they form a detailed data set for differential high-energy electron and proton measurements and are used in this study. A data analysis method for discerning proton deposits from PHA data has been described previously [*Selesnick et al.*, 2014] and is here adapted for electron data.

REPTile is a simplified and miniaturized version of REPT and has a robust design verified with Geometry and Tracking 4 (Geant4) simulations [*Agostinelli et al.*, 2003; *Schiller and Mahendrakumar*, 2010; *Li et al.*, 2013b]. Since CSSWE is in a highly inclined (65°) low Earth orbit, 480 km × 780 km, CSSWE traverses the radiation belts 4 times in each orbit (~ 1.5 h), providing a global view of their spatial structure [*Li et al.*, 2013b]. Figure 1 shows energetic electron and proton fluxes in REPTile's first two energy channels plotted versus geographic longitude and latitude for a 4 day interval, 10–14 January 2013. The electrons are seen in a two-belt structure, with inner belt only seen above the South Atlantic Anomaly (SAA) region, where the Earth's magnetic field is weak. The outer belt lower energy electrons, 0.58–1.63 MeV, penetrate into the lower latitude or lower L, which represents the geocentric distance in R_E at the equator of the shell if the Earth's magnetic field is approximated as a dipole, and some of them seem to merge with the inner belt, visible in the south of SAA region. The higher-energy electrons, 1.63–3.8 MeV, seem to be clearly separated from the inner belt. There are no solar energetic particle events during this period nor are any energetic protons detected in the outer belt. Energetic protons are thus detectable only when above the SAA region. A few points are worth noting here: (1) the intensity of 9–18 MeV protons is lower than 18–30 MeV protons, which is consistent with previous finding [*Selesnick et al.*, 2007], due to the faster loss of lower energy protons created by CRAND; (2) the lower energy electrons are in a much wider region around the SAA, and their flux is orders of magnitude higher than the proton flux in the SAA, demonstrating an abundance

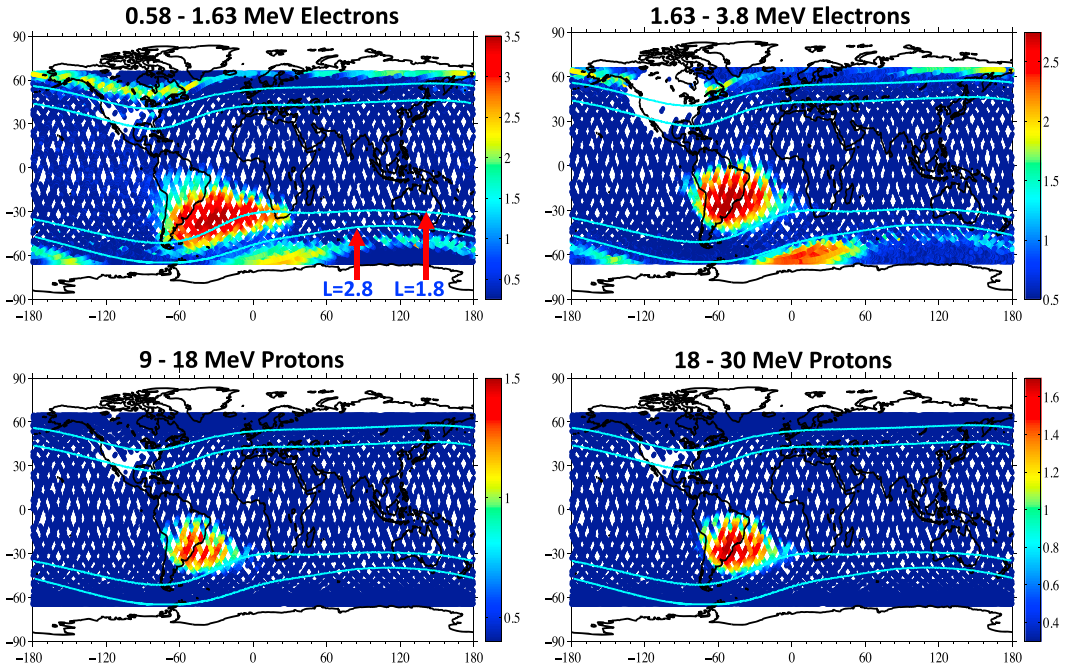

Figure 1. Mercator map of electron and proton fluxes from the first two energy channels of REPTile during 10–14 January 2013.

of such low-energy electrons in the inner belt as well as in the slot region; (3) the higher-energy electrons show a similar shape and flux level in the SAA as the protons, suggesting that the proton contamination can be significant for the higher-energy channel. Such similarity remains the same for some more active period, such as in the middle of October 2012 [*Li et al.*, 2013b], while the outer belt electrons can be much different. Thus, we should look at these issues more carefully.

Figure 2 shows measurements of these two channels taken in the Southern Hemisphere (blue) and Northern Hemisphere (red) as a function of the magnetic longitude for a longer period, 4–14 January 2013, for better statistics. As the electrons drift eastward, they are subjected to pitch angle scattering. Electrons that can be measured by REPTile in the north will precipitate into atmosphere in the SAA because their corresponding mirroring points would be below 100 km altitude.

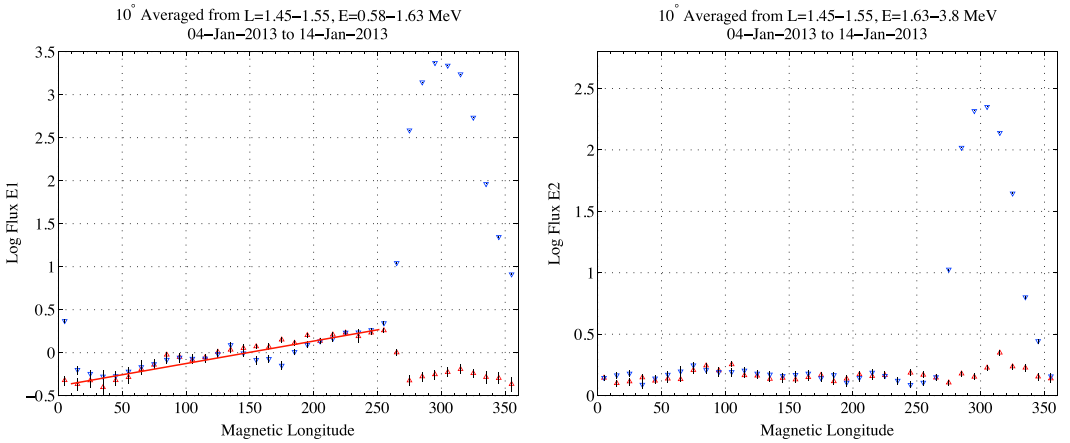

Figure 2. REPTile measurements around $L = 1.7$ in the Southern Hemisphere (blue) and Northern Hemisphere (red) versus magnetic longitude for the time period of 4–14 January 2013. The red line on the left figure guides the slope, which suggests a weak pitch angle diffusion as the electrons drift toward the South Atlantic Anomaly region, >250°.

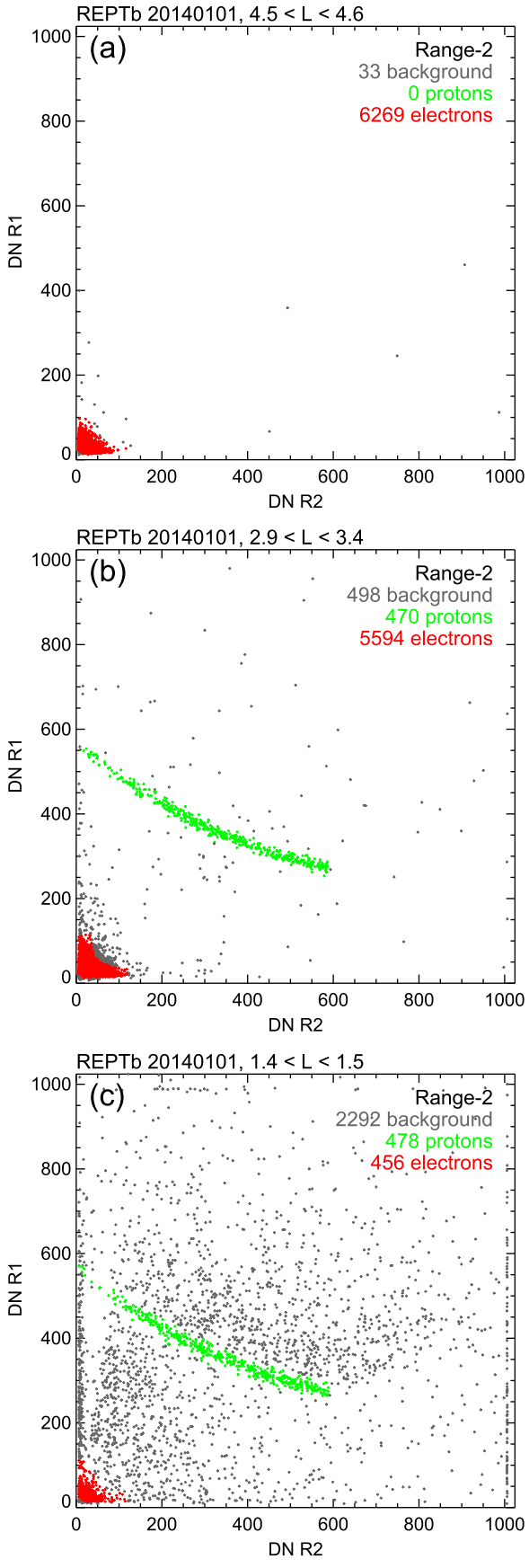

In the drift loss cone (DLC, longitudes <250°) the lower energy E1 channel measurements show increasing flux (red line) as quasi-trapped electrons drift eastward. This is caused by large-angle, nondiffusive, pitch angle scattering of stably trapped electrons from Coulomb collisions with atmospheric neutral atoms, plasma ions, and free electrons [*Selesnick*, 2012]. Flux increases eastward during the time, ~1 h, required to drift through the DLC before reaching the SAA (longitudes >250°), where electrons are lost in the dense atmosphere and where higher fluxes of stably trapped electrons are seen in the figure. Similar flux variations in outer belt electron data are caused by weak pitch angle diffusion from scattering by plasma waves [*Selesnick*, 2006; *Tu et al.*, 2010]. Similar variations should also be expected for the higher-energy channel from REPTile in the inner belt if it also measures quasi-trapped electrons in the DLC and stably trapped electrons in the SAA. However, the E2 channel data in Figure 2 do not show such a pattern, casting doubt on the existence of such high-energy electrons (>1.6 MeV) in the inner belt.

The question is how to quantify the high-energy electron flux in the inner belt or at least find an upper limit. This will be the main focus of the following based on REPT measurements.

3. Particle Identification in REPT Measurements

Examples of PHA data taken by REPT-B (on the RBSP-B spacecraft) during a single day (1 January 2014) are shown in Figure 3. Data numbers (DN)

Figure 3. REPT pulse height data for Range-2 events from a single day, 1 January 2014. The DN values from R1 and R2 are proportional to energy deposited in those detectors. Three *L* shell ranges represent (a) the outer belt electron peak, (b) the inner edge of outer belt electrons and outer edge of inner belt protons, and (c) the inner belt proton peak. Preliminary event identification, as described in the text, is indicated by color for protons (green), electrons (red), and background (gray). The number of events of each type in each *L* range is indicated.

proportional to energy loss, Δ, in a given detector, where Δ in MeV is ~ DN/38 (the exact value varies between detectors and spacecraft). Figure 3 shows DN from the front detector (R1) versus DN from the second detector (R2), for so-called Range 2 events (events in which only the first two detectors were triggered and both had nonzero DN). Data are also separated by L: (a) $4.5 < L < 4.6$, near the outer zone electron peak; (b) $2.9 < L < 3.4$, near the inner edge of the electron outer zone and the outer edge of the proton inner zone; and (c) $1.4 < L < 1.5$, near the inner zone proton peak.

In Figure 3, events are nominally identified as protons (green), electrons (red), or background (gray). Similar identification is made for events with higher ranges, for which data from more detectors are available. To be considered a valid Range n proton or electron event there must be a high probability that the particle was in the REPT field of view (FOV), entered the detector stack at R1, and stopped in detector Rn. Low probability, or background, events can result from high-energy protons that were outside the FOV, or perhaps from electrons in the FOV that scattered out of the detector stack. The valid Range 2 events of Figure 3 have kinetic energies ~20 to 30 MeV for protons and ~1.5 to 3 MeV for electrons before passing through the 2 mm Be window (at the front of the detector stack) and R1 and finally stopping in R2.

The probability density function (PDF) for energy loss Δ in a path length x from an incident energy E is called the straggling function, $f(\Delta, E, x)$ [*Bichsel*, 1988]. The probability of a valid Range n event is given by the following product:

$$f_{n-1}(E,\theta) = \prod_{i=1}^{n-1} f(\Delta_i, E - E_{i-1}, x_i \sec\theta) \tag{1}$$

where the straggling function f is the probability density for measured energy loss Δ_i in detector i of thickness x_i with incident angle θ. The incident energy E (after going through the Be window) at R1 is reduced by the total energy loss up to detector i:

$$E_{i-1} = \sum_{j=1}^{i-1} \Delta_j \tag{2}$$

The straggling function $f(\Delta, E, x \sec\theta)$ may also be viewed as the distribution of energy deposits Δ that would be measured in a detector of thickness x from many particles all with the same incident energy E and angle θ. It represents the probability of a particular Δ given E and θ, or, equivalently, of a particular E and θ given Δ. Since the energy deposits Δ_i measured by consecutive detectors in REPT are independent random processes, the product of probabilities, f_{n-1}, in equation (1) is the probability of a particular E and θ given a set of measured Δ_i. This probability depends on the assumed type of incident particle, proton, or electron, because the straggling functions are different for each. Therefore, by evaluating f_{n-1} separately for each particle type, the probabilities that a given event corresponded to an incident proton or electron are determined. If one of the probabilities is above a certain threshold, e.g., $f_{\min} \sim 10^{-3}$ in the Range 2 event for either protons or electrons, then it is counted as a particle of that type. If neither of the probabilities are above the threshold, then it is a background event. (It never occurs that both probabilities are above the threshold because the proton and electron regions shown in Figure 3 do not overlap.)

For protons, accurate approximations are available for the straggling function [*Selesnick et al.*, 2014] and f_{n-1} is evaluated at the incident energy for a particle stopping in detector n, $E = E_n$, and for the mean incident angle $\bar{\theta}$ over the distribution $f_{n-1}(E_n, \theta)$.

Electrons can scatter significantly in the detector stack, and the incident angle at each detector is likely to vary. Evaluation of f_{n-1} is therefore more complex. However, a simplified approach was adopted for the task of electron identification by assuming the following: incident angle $\theta = 0$ at each detector, and the straggling function f is the universal Landau distribution [*Schorr*, 1974], which is accurate in the limiting case of thin detectors. Because the method is used only for identification of candidate electron events, the validity of this simplified approach is determined by its accuracy in cases where nearly all events are known to be electrons.

For the outer zone region represented in Figure 3a, as expected, no valid proton events are identified and virtually all of the Range 2 events are identified as valid electrons. The small fraction of background events may result from cosmic rays.

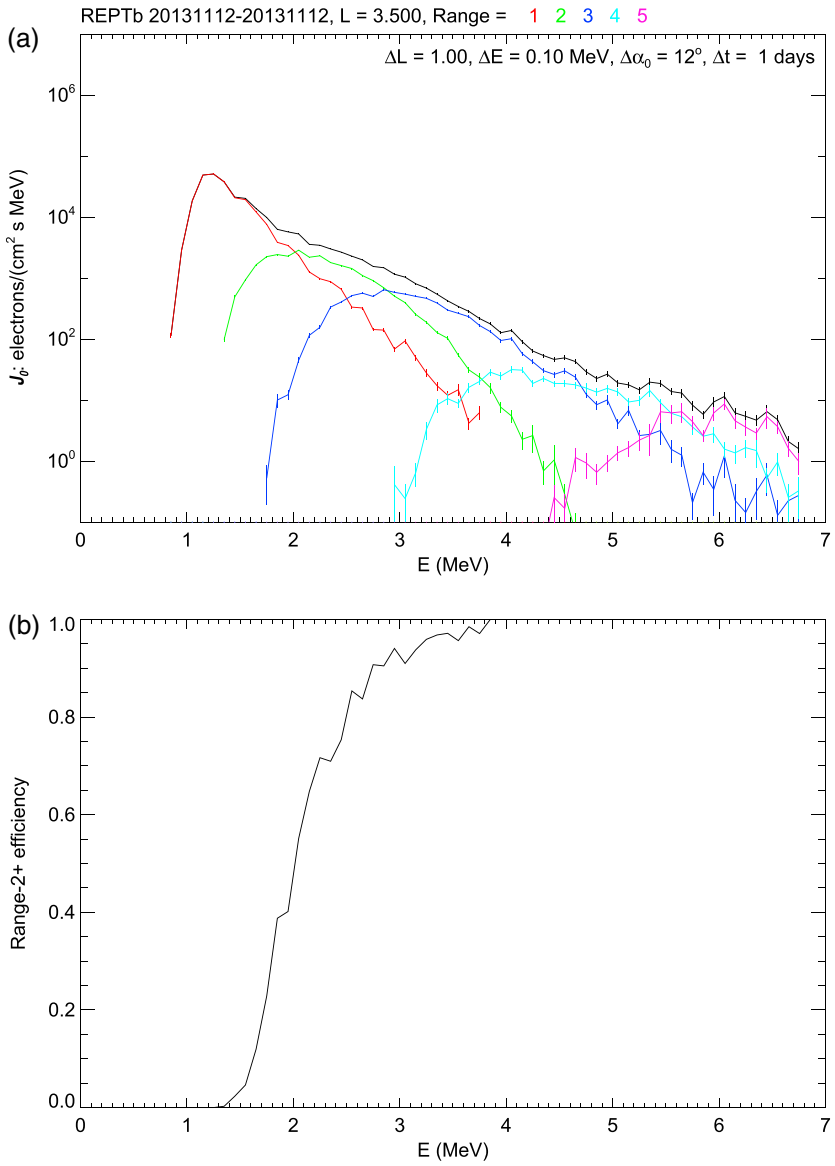

Figure 4. (a) Average omnidirectional equatorial electron energy spectrum (black) from REPT PHA data for $3 < L < 4$ during 11 November 2013. Color-coded contributions from each Range 1 through 5 are also shown. Bin widths used in the data analysis are listed. (b) Derived electron detection efficiency excluding the Range 1 data.

For the medium *L* region represented in Figure 3b, both inner zone protons and outer zone electrons are identified. The background is higher, caused by protons outside the FOV and perhaps also by electrons that were not properly identified. However, as in Figure 3a, most of the candidate electron events were identified as valid, justifying the simplified approach described above. Very few proton events, or background events of indeterminate origin, were incorrectly identified as electrons, which have a very different energy deposit pattern. The low number of background events, relative to the number of valid electron events, leaves little doubt that most of the events are properly identified in this case.

For the inner zone, Figure 3c, valid proton and electron events are identified, but most of the PHA events are background caused by intense high-energy protons. These protons can penetrate the thick shielding, outside the FOV, that stops lower energy protons and electrons. Some background events are in close proximity, by DN value, to the identified electron events. Therefore, their classification as electrons is now dubious and should be confirmed or refuted by other means, as discussed in detail below.

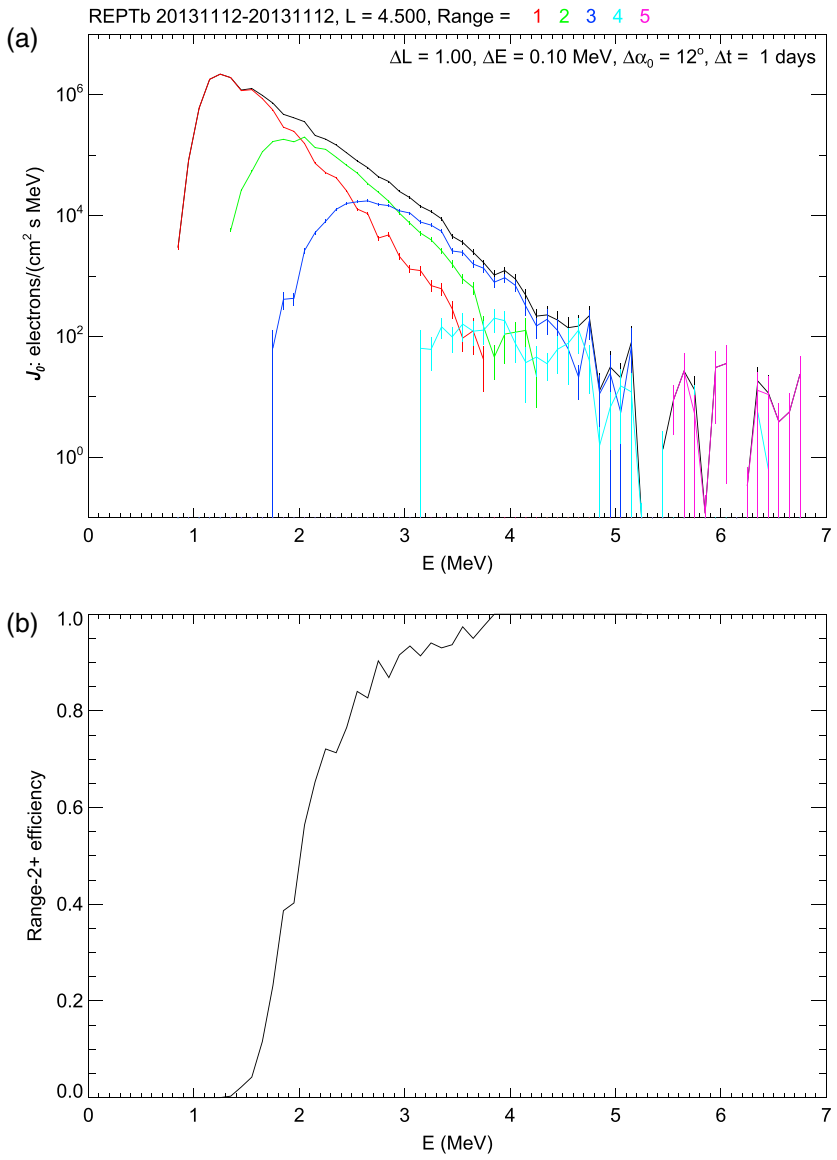

Figure 5. Similar to Figure 4 but for $4 < L < 5$.

4. Energy Spectra of REPT Measurements

After valid PHA events have been identified, computation of particle intensity as a function of energy and pitch angle is straightforward for protons [*Selesnick et al.*, 2014], because the detection efficiency in the FOV is near unity. For electrons, scattering can reduce the detection efficiency. However,the REPT design minimizes scattering effects [*Baker et al.*, 2012] and the same method for computing particle intensity is adapted here for electrons.

Outer zone electron omnidirectional differential energy spectra are shown in Figures 4a and 5a (black traces), averaged over the ranges $3 < L < 4$ and $4 < L < 5$, respectively. They are from REPT-A and REPT-B data combined and averaged over a 1 day interval (12 November 2013). Also shown are separate contributions to the total from the individual ranges $n = 1$ to 5 (colored traces). Range 1 events, for which only detector R1 is triggered, are useful in the outer zone, where it is safe to assume that all events are due to electrons. They provide a lower energy threshold than the Range 2 or greater events that are represented in the nominal energy ranges of REPT [*Baker et al.*, 2012].

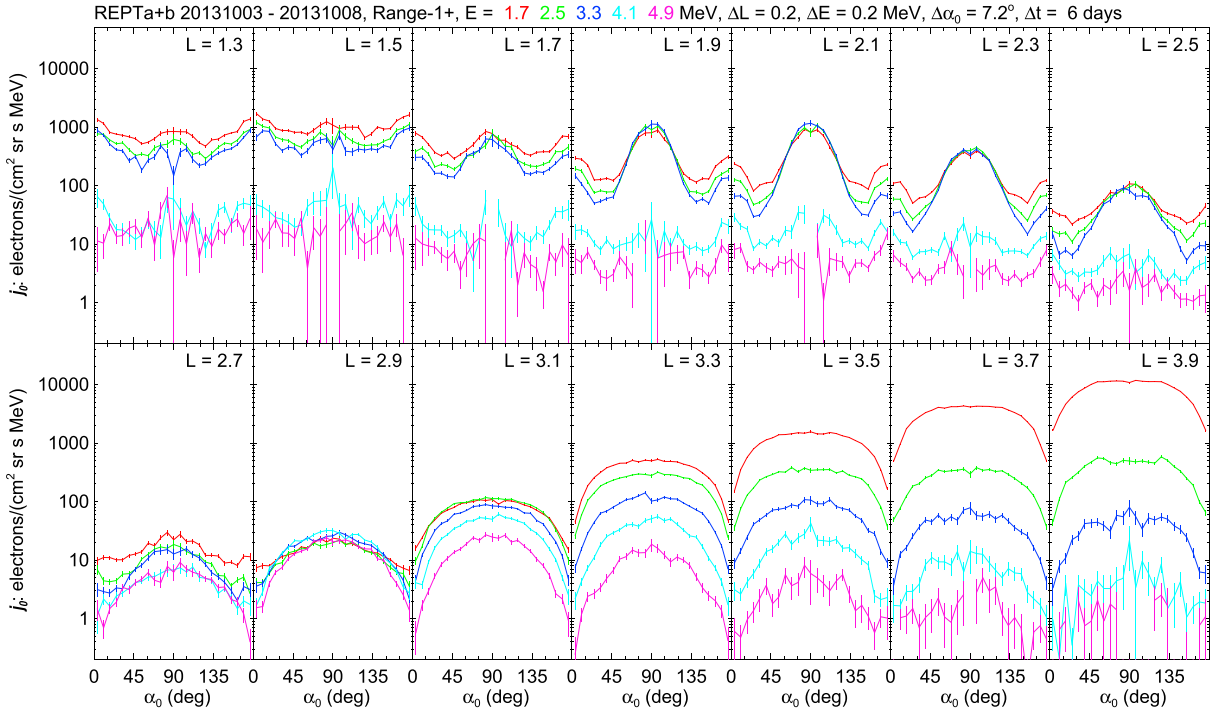

Figure 6. Average equatorial pitch angle distributions derived from REPT PHA events identified tentatively as electrons in Ranges 1 through 5, for separate *L* values from 1.3 to 3.9, during 3 through 8 October 2013. Electron energies are color coded. Bin widths used in the data analysis are listed.

For the inner zone, Range 1 data are less useful for electron measurements because of the intense high-energy proton population, which can penetrate shielding outside the FOV and trigger R1 but not R2 and beyond. However, the ratio of outer zone spectra calculated with and without the Range 1 data (red line in Figures 4a and 5a) provides an efficiency factor for correcting intensities calculated from Range 2 and above, extending their utility to lower energies. This efficiency factor is shown in Figures 4b and 5b. Despite the harder energy spectrum at lower $L(=3.5)$, the efficiency factors from the two L ranges (3.5 and 4.5) are in close agreement. They extend the useful energies of the Range 2 electron data down to ~1.5 MeV in the outer zone. However, Range 2 and beyond data are still to be tested in the inner zone, as to be described in the next section.

5. Pitch Angle Distributions

Van Allen Probes satellites are oriented such that the spin axis is roughly in the sunward direction, with a spin period of ~12 s. Directional differential intensity, from PHA events nominally identified as electrons, is shown in the form of equatorial pitch angle distributions (PADs) at selected L and E values in Figures 6 and 7. Data are from REPT-A and REPT-B data combined and averaged over a 6 day interval (3–8 October 2013). Figure 6 includes data from Ranges 1 to 5 events; Figure 7 includes only Ranges 2 to 5 events but uses the efficiency from Figure 5b (Figure 4b gives essentially the same efficiency) as a correction factor for the lower energies. For the lower energies, E = 1.7, 2.5, and 3.3 MeV, Figure 6 includes the Range 1 data but Figure 7 does not. The smaller number of events used in Figure 7 is combined with a smaller efficiency factor to determine electron intensities, which should thereby agree with those of Figure 6.

For the outer zone, $L \geq 3$, Figures 6 and 7 are indeed in close agreement as expected from data dominated by electrons. Distributions are characteristic of trapped electrons, with broad maxima near equatorial pitch angle $\alpha_0 = 90°$ and minima associated with the loss cones at $\alpha_0 = 0$ and 180° (loss cones are not fully resolved because of the 32° FOV).

For the inner zone, $L \leq 3$, there is strong disagreement between Figures 6 and 7. Distributions narrowly peaked at $\alpha_0 = 90°$ from the Range 1 data ($1.7 \leq L \leq 2.5$ in Figure 6) result from high-energy protons with degraded energy deposits in R1 (likely from skimming the edge of R1 and masquerading as electrons),

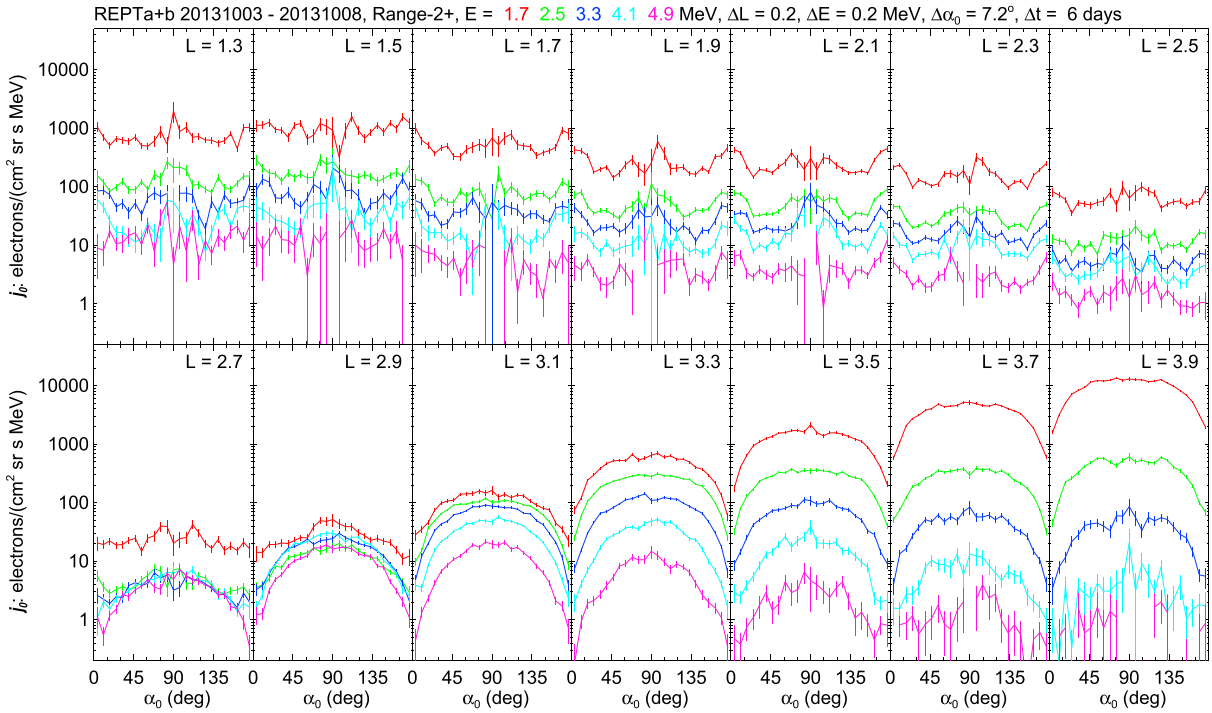

Figure 7. Similar to Figure 6 but from PHA data in Ranges 2 through 5 only.

as confirmed by comparison with reliable measurement of the proton pitch angle distributions [*Selesnick et al.*, 2014]. Clearly, the Range 1 data should not be used for inner zone electron measurements. In fact, all REPT data that are publicly available do not include any Range 1 data. Here the Range 1 data are shown in comparison with Range 2 data as a test of both data types.

The results from excluding Range 1 data (Figure 7) do not show such clear inner zone proton contamination, but neither are the distributions characteristic of trapped electrons. Within statistical uncertainties, they are essentially isotropic for $L \leq 2.7$. Loss cones widen with decreasing L, with widths ~60° at the lowest L values [*Selesnick et al.*, 2014]. That prominent loss cones are not evident in the inner zone pitch angle distributions suggests that the measured electron intensities there are results of contamination. The likely explanation is that the intensity of any high-energy electrons that may be present is dominated by the background caused by inner zone protons (Figure 3c). The background events can result from relativistic (≥500 MeV) protons, that leave low-energy deposits thus mimicking electrons, or from degraded energy deposits of lower energy protons. In either case, the proton energies are high enough (≥100 MeV) to penetrate the shielding around REPT and enter the detector stack at large angles to the telescope axis (rare nuclear scattering events in the detector stack may also contribute to the background). The pitch angle distributions therefore appear isotropic even though the protons themselves are in trapped distributions [*Selesnick et al.*, 2014].

6. Time Dependence

Omnidirectional differential intensity, from Range 2 and greater PHA events nominally identified as electrons, is shown as a function of L and time in Figure 8, for (a) $E = 2.1$ MeV and (b) $E = 4.9$ MeV. Data are from REPT-A and REPT-B data combined and averaged over 2 day intervals from October 2013 to March 2014.

For $L \geq 2.6$ there are intensity variations at both energies that are characteristic of outer zone electrons. Near the start of the interval, higher-energy electrons near $L = 3$ are unusually intense (Figure 8b), as seen also in the PADs (Figure 6 or 7), but decay with time.

For $L \leq 2.6$ the inner zone intensities are stable over time for both energies, apart from statistical fluctuations. It has already been seen that the inner zone data are dominated by proton background at

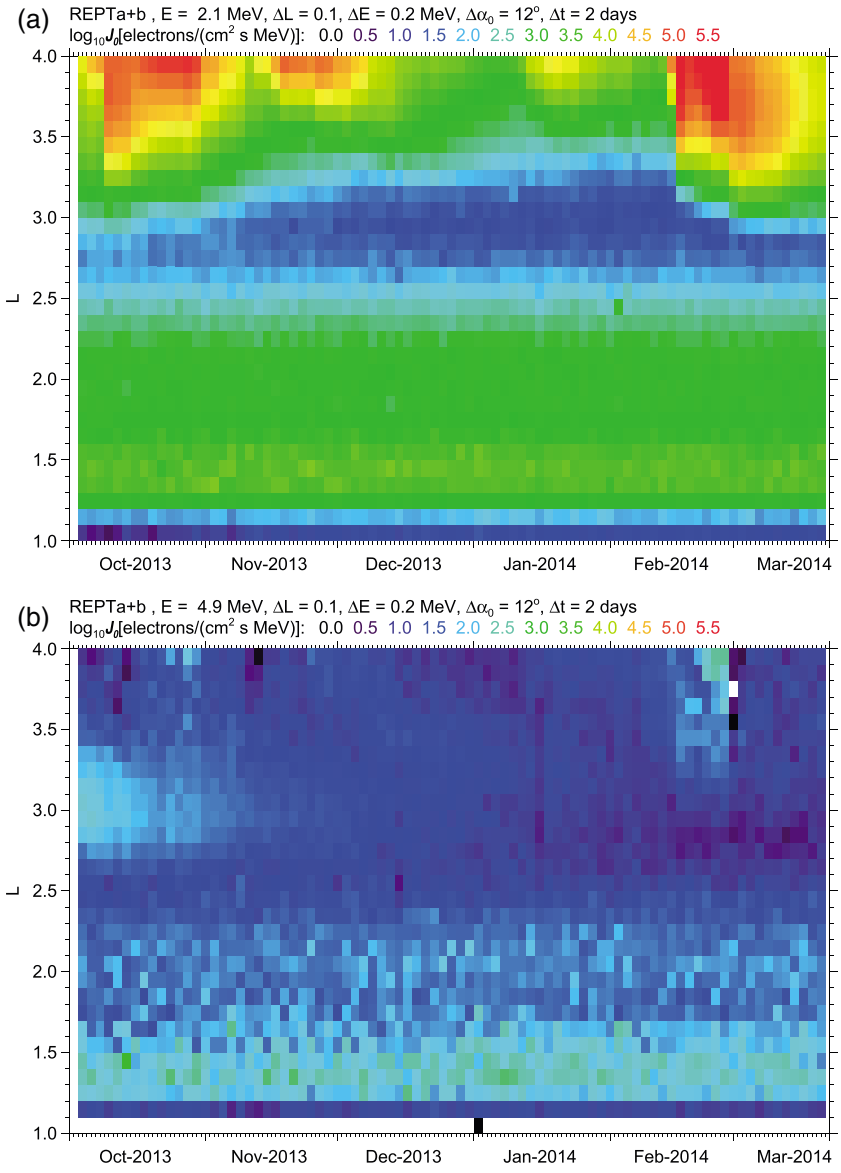

Figure 8. Color-coded omnidirectional equatorial intensity of REPT PHA events identified tentatively as electrons versus *L* and time for electron energies of (a) 2.1 MeV and (b) 4.9 MeV. Bin widths used in the data analysis are listed.

the start of the interval. Since there were no clear injections of high-energy electrons, the same conclusion applies throughout the interval.

7. Upper Limits

Omnidirectional differential intensity, from Range 2 and greater PHA events nominally identified as electrons, is shown as a function of *L* for selected energies in Figure 9. Data are from REPT-A and REPT-B data combined and averaged over a 6 day interval (3–8 October 2013), as in Figure 7. Inner zone regions where pitch angle distributions show that the data are in fact dominated by proton background are indicated (dashed lines in the figure). They vary from $L < 2.8$ for $E = 1.7$ MeV to $L < 2.5$ for $E = 4.9$ MeV, the higher energies being more reliable because proton background is lower when more detectors are triggered. The conclusion that the data are dominated by proton background is supported by the strong resemblance of the *L* distributions to those observed for trapped protons during the same time interval [*Selesnick et al.*, 2014]. In these inner zone regions the measured intensities should be considered upper limits on the actual trapped electron intensity.

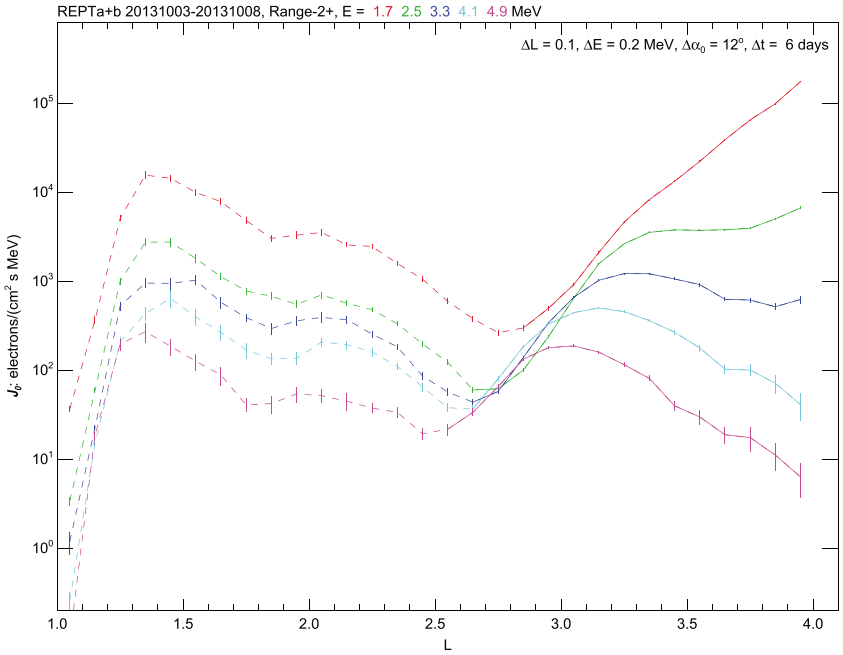

Figure 9. Average omnidirectional equatorial intensity of REPT PHA events identified tentatively as electrons versus L during 3 through 8 October 2013, for selected color-coded electron energies. Dashed lines indicate where the identification is considered unreliable and the data likely result from high-energy protons.

Electron omnidirectional differential intensity from the AE8 and AE9 empirical models are shown as a function of L in Figure 10, at the same selected energies as in Figure 9. The modeled inner zone peak intensity near $L = 1.5$ is seen to be significantly higher than the upper limits derived from REPT data, at least for $E \leq 3$ MeV.

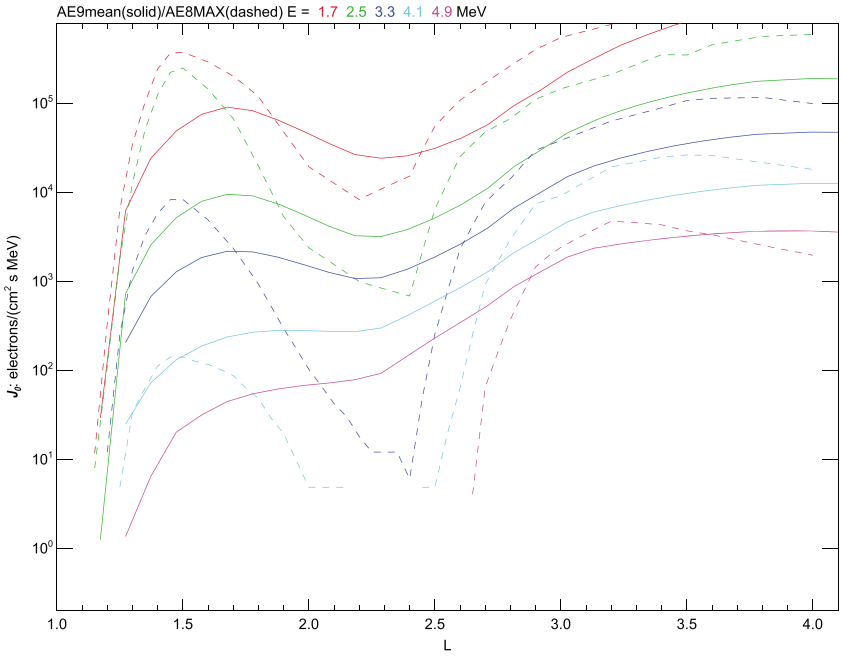

Figure 10. Omnidirectional equatorial electron intensity from the AE8MAX (dashed lines) and AE9 V1.2 (solid lines) radiation belt models, in the same format as Figure 9. The AE8MAX (solar maximum) model differs from the AE8MIN (solar minimum) model only for $L > 2.5$. For the AE9 model, mean values are shown.

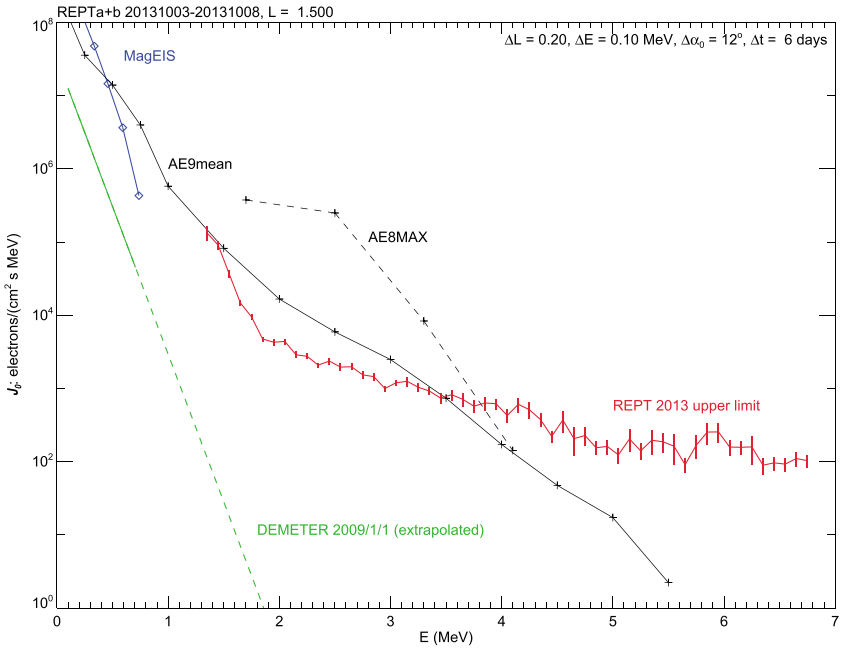

Figure 11. Omnidirectional equatorial electron energy spectra at $L = 1.5$. The average spectrum derived from REPT PHA data (red) likely results from high-energy protons rather than electrons and therefore is an upper limit on the actual electron intensity. Bin widths used in the data analysis are listed. Equivalent model spectra from AE9 V1.2 (solid black) and AE8MAX (dashed black) are shown for comparison. Also shown are MagEIS data (blue) of selected energy channels during the period of 24 February to 1 March 2013 and the exponential energy spectrum measured on the low-altitude (not equatorial) DEMETER satellite during January 2009 for $E < 0.8$ MeV (solid green) and extrapolated to higher energies (dashed green).

The derived upper limit on the omnidirectional differential intensity for $L = 1.5$ is shown as a function of E in Figure 11 (red line). The intensity from the AE8 (dashed black line) and AE9 (black line) models are shown for comparison. Also shown are MagEIS data (blue) of selected energy channels during the period of 24 February to 1 March 2013 and an exponential energy spectrum (green line) derived from data taken on the low-altitude DEMETER satellite during 2009 [*Selesnick*, 2012]. Those are reliable measurements of electron intensity for $E < 800$ keV, and an extrapolation to higher energies (dashed green line) is well below the upper limits derived from REPT data.

8. Discussion

There are abundant sub-MeV electrons in the inner radiation belt, as demonstrated by CSSWE/REPTile measurements shown in Figures 1 and 2. These are consistent with previous studies using DEMETER measurements: (1) *Selesnick* [2012] modeled the precipitation loss of hundreds of keV electrons during the quiet year of 2009 and concluded that significant inward radial diffusion must be taking place to replenish the electron population, (2) *Zhao and Li* [2013a] modeled fast injections of hundreds of keV electrons during a more active year of 2001 and concluded that the fast enhancements of the electrons in the inner belt can be modeled by inward radial diffusion but the diffusion coefficients must be greater and more dynamic than what is commonly thought. However for MeV electrons, it is much more difficult to transport them inward, which is also illustrated and discussed in a recent paper by *Baker et al.* [2014].

Also the high-quality measurements of the Magnetic Electron Ion Spectrometer, MagEIS, instrument [*Blake et al.*, 2013] onboard Van Allen Probes, which was designed so it could correct for proton backgrounds in the inner zone, enabled detailed studies of the PADs of $\leq$ 600 keV electrons in the inner belt, and *Zhao et al.* [2014a, 2014b] described unusual PADs there that 90 minimum PADs dominate during injection times and normal PADs dominate during quiet times. It is clear that these $\leq$ 600 keV electrons have fluxes significantly higher than the background noise.

Fennell et al. [2015] have shown that the energy spectrum of relativistic electrons in the inner belt is very steep and the flux of ≥ 800 keV electrons are already at the background noise level of the MagEIS, while the flux of < 400 keV electrons is even higher than the AE9 mean value as shown in Figure 11.

However, AE8 and AE9 predict much higher MeV electron fluxes (< 3 MeV) in the inner belt than the upper limit bounded by REPT. We can provide two explanations for the discrepancies: (1) the models are based on data from early years when there had been more deep injections of MeV electrons [*Blake et al.*, 1992; *Baker et al.*, 2004] and there have not been any events as strong as those in terms of interplanetary shock speed and geomagnetic storm intensity in the years just before and during the Van Allen Probes era; and (2) the proton contamination on previous data used for the model building may not have been removed properly.

REPT represents a state-of-art instrument for accurately measuring the energetic particles in the magnetosphere—both REPT instruments on the twin Van Allen Probes show identical features throughout their entire orbits, including the outer belt, slot region, and the inner belt. This, supported by the high-quality measurements of the MagEIS instruments that show no measurable >800 keV electrons in the inner belt [*Fennell et al.*, 2015], leaves little doubt that the upper limits of MeV electrons bounded by REPT measurements should be the standard for future model improvement, at least for periods like the last few years when no extreme solar wind conditions were observed.

9. Conclusion

Concurrent measurements of relativistic electrons by REPTile and REPT have been analyzed with the focus on the upper limit of MeV electrons in the inner belt. While there are abundant sub-MeV electrons (<600 keV) in the inner belt, the intensity of >1 MeV electrons can only be bounded by upper limits (the actual MeV electron flux level is likely much lower), which are significantly lower than intensity levels predicted by AE8 and AE9 models. This finding is significant for two reasons: (1) it shows that unless there are extreme solar wind conditions, such as strong interplanetary shocks and large coronal mass ejections, which have not happened yet since the launch of Van Allen Probes, significant enhancements of MeV electrons do not occur in the inner belt even though such enhancements are commonly seen in the outer belt; and (2) it also suggests that deep dielectric discharging due to MeV electrons is not a concern for satellites in the inner belt region, at least not during the phase of solar cycle where strong interplanetary shocks and large coronal mass ejections are much less likely.

Acknowledgments

We thank Bob Johnston for help with the AE9 V1.2 model. This work was supported in part by NASA agreement NNH14AX18I with the Air Force Research Laboratory under the Heliophysics Guest Investigators Program, at University of Colorado by RBSP-ECT funding through JHU/APL contract 967399 under prime NASA contract NAS5-01072, NSF (CubeSat program) grant AGSW 0940277, and a subcontract (FA9453-14-M-0256) from the Air Force Research Laboratory. Van Allen Probes REPT and ephemeris data are available from the ECT Science Operations and Data Center, http://www.rbsp-ect.lanl.gov; CSSWE/REPTile and ephemeris data are available from NASA/CDAWeb database, http://cdaweb.gsfc.nasa.gov/istp$_$public/.

Yuming Wang thanks the reviewers for their assistance in evaluating this paper.

References

Agostinelli, S., et al. (2003), Nuclear instruments and methods in Physics Research section A: Accelerators, spectrometers, detectors and associated equipment, *Nucl. Instrum. Methods Phys. Res., Sect. A*, *506*, 250–303.

Baker, D. N., S. G. Kanekal, X. Li, S. P. Monk, J. Goldstein, and J. L. Burch (2004), An extreme distortion of the Van Allen belt arising from the 'Halloween' solar storm in 2003, *Nature*, *432*, 878–881, doi:10.1038/nature03116.

Baker, D. N., S. G. Kanekal, R. B. Horne, N. P. Meridith, and S. A. Glauert (2007), Low-altitude measurements of 26 MeV electron trapping lifetimes at $1.5 \leq L \leq 2.5$, *Geophys. Res. Lett.*, *34*, L20110, doi:10.1029/2007GL031007.

Baker, D. N., et al. (2012), The Relativistic Electron-Proton Telescope (REPT) instrument on board the Radiation Belt Storm Probes (RBSP) spacecraft: Characterization of Earth's radiation belt high-energy particle populations, *Space Sci. Rev.*, *179*, 337–381, doi:10.1007/s11214-012-9950-9.

Baker, D. N., et al. (2014), An impenetrable barrier to ultra-relativistic electrons in the Van Allen radiation belt, *Nature*, *515*, 531–534, doi:10.1038/nature13956.

Blake, J. B., W. A. Kolasinski, R. W. Fillius, and E. G. Mullen (1992), Injection of electrons and protons with energies of tens of MeV into L < 3 on March 24, 1991, *Geophys. Res. Lett.*, *19*, 821–824, doi:10.1029/92GL00624.

Blake, J. B., et al. (2013), The Magnetic Electron Ion Spectrometer (MagEIS) instruments aboard the radiation belt storm probes (RBSP) spacecraft, *Space Sci. Rev.*, *179*(1–4), 383–421, doi:10.1007/s11214-013-9991-8.

Bichsel, H. (1988), Straggling in thin silicon detectors, *Rev. Mod. Phys.*, *60*, 663–699, doi:10.1103/RevModPhys.60.663.

Funstein, H. O., et al. (2013), Helium, Oxygen, Proton, and Electron (HOPE) mass spectrometer for the radiation belt storm probes mission, *Space Sci. Rev.*, *179*, 423–484, doi:10.1007/s11214-013-9968-7.

Fennell, J. F., S. G. Claudepierre, J. B. Blake, T. P. O'Brien, J. H. Clemmons, D. N. Baker, H. E. Spence, and G. D. Reeves (2015), Van Allen Probes show the inner radiation zone contains no MeV electrons: ECT/MagEIS data, *Geophys. Res. Lett.*, doi:10.1002/2014GL062874.

Ginet, G. P., et al. (2013), AE9, AP9 and SPM: New models for specifying the trapped energetic particle and space plasma environment, *Space Sci. Rev.*, *179*, 579–615, doi:10.1007/s11214-013-9964-y.

Horne, R. B., et al. (2005), Wave acceleration of electrons in the Van Allen radiation belts, *Nature*, *437*, 227–230, doi:10.1038/nature03939.

Kessel, R. L., N. J. Fox, and M. Weiss (2012), The Radiation Belt Storm Probes (RBSP) and space weather, *Space Sci. Rev.*, *179*, 531–543, doi:10.1007/s11214-012-9953-6.

Kim, K.-C., and Y. Shprits (2012), Radial gradients of phase space density in the inner electron radiation, *J. Geophys. Res.*, *117*, A12209, doi:10.1029/2012JA018211.

Kress, B. T., M. K. Hudson, M. D. Looper, J. Albert, J. G. Lyon, and C. C. Goodrich (2007), Global MHD test particle simulations of >10 MeV radiation belt electrons during storm sudden commencement, *J. Geophys. Res.*, *112*, A09215, doi:10.1029/2006JA012218.

Li, X., and M. A. Temerin (2001), The electron radiation belt, *Space Sci. Rev.*, *95*(1–2), 569–580, (a solicited review paper).

Li, X., I. Roth, M. Temerin, J. Wygant, M. K. Hudson, and J. B. Blake (1993), Simulation of the prompt energization and transport of radiation particles during the March 24, 1991 SSC, *Geophys. Res. Lett.*, *20*, 2423–2426, doi:10.1029/93GL02701.

Li, X., A. B. Barker, D. N. Baker, W. C. Tu, T. E. Sarris, R. S. Selesnick, R. Friedel, and C. Shen (2009), Modeling the deep penetration of outer belt electrons during the "Halloween" magnetic storm in 2003, *Space Weather*, *7*, S02004, doi:10.1029/2008SW000418.

Li, X., S. Palo, R. Kohnert, D. Gerhardt, L. Blum, Q. Schiller, D. Turner, W. Tu, N. Sheiko, and C. S. Cooper (2012), Colorado Student Space Weather Experiment: Differential flux measurements of energetic particles in a highly inclined low Earth orbit, in *Dynamics of the Earth's Radiation Belts and Inner Magnetosphere, Geophys. Monogr. Ser.*, vol. 199, edited by D. Summers, pp. 385–404, AGU, Washington, D. C., doi:10.1029/2012GM001313.

Li, X., S. Palo, R. Kohnert, L. Blum, D. Gerhardt, Q. Schiller, and S. Califf (2013a), Small mission accomplished by students—Impact on space weather research, *Space Weather*, *11*, 55–56, doi:10.1002/swe.20025.

Li, X., et al. (2013b), First results from CSSWE CubeSat: Characteristics of relativistic electrons in the near-Earth environment during the October 2012 magnetic storms, *J. Geophys. Res. Space Physics*, *118*, 6489–6499, doi:10.1002/2013JA019342.

Lenchek, A. M., S. F. Singer, and R. C. Wentworth (1961), Geomagnetically trapped electrons from cosmic ray albedo neutrons, *J. Geophys. Res.*, *66*(12), 4027–4046, doi:10.1029/JZ066i012p04027.

Lyons, L. R., and R. M. Thorne (1973), Equilibrium structure of radiation belt electrons, *J. Geophys. Res.*, *78*, 2142–2149, doi:10.1029/JA078i013p02142.

Looper, M. D., J. B. Blake, R. A. Mewaldt, J. R. Cummings, and D. N. Baker (1994), Observations of the remnants of the ultrarelativistic electrons injected by the strong SSC of 24 March 1991, *Geophys. Res. Lett.*, *21*, 2079–2082, doi:10.1029/94GL01586.

Mauk, B. H., N. J. Fox, S. G. Kanekal, R. L. Kessel, D. G. Sibeck, and A. Ukhorskiy (2012), Science objectives and rationale for the radiation belt storm probes mission, *Space Sci. Rev.*, *179*, 3–27, doi:10.1007/s11214-012-9908-y.

Rosen, A., and N. L. Sanders (1971), Loss and replenishment of electrons in the inner radiation zone during 1965–1967, *J. Geophys. Res.*, *76*(1), 110–121, doi:10.1029/JA076i001p00110.

Vette, J. I. (1991), The AE-8 trapped electron model environment, *NSSDC/WDC-A-R&S 91–24*, NASA Goddard Space Flight Center, Greenbelt, Md.

Schiller, Q., and A. Mahendrakumar (2010), REPTile: A miniaturized detector for a CubeSat mission to measure relativistic particles in near-Earth space, paper SSC10-VIII-1 presented at 24th Annual AIAA/USU Conference on Small Satellites, Frank J. Redd Student Scholarship Competition, Logan, Utah, USA, Aug. 9-12, 2010.

Schorr, B. (1974), Programs for the Landau and the Vavilov distributions and the corresponding random numbers, *Comput. Phys. Commun.*, *7*, 215–224.

Selesnick, R. S. (2006), Source and loss rates of radiation belt relativistic electrons during magnetic storms, *J. Geophys. Res.*, *111*, A04210, doi:10.1029/2005JA011473.

Selesnick, R. S. (2012), Atmospheric scattering and decay of inner radiation belt electrons, *J. Geophys. Res.*, *117*, A08218, doi:10.1029/2012JA017793.

Selesnick, R. S., D. N. Baker, A. N. Jaynes, X. Li, S. G. Kanekal, M. K. Hudson, and B. T. Kress (2014), Observations of the inner radiation belt: CRAND and trapped solar protons, *J. Geophys. Res. Space Physics*, *119*, 6541–6552, doi:10.1002/2014JA020188.

Selesnick, R. S., M. D. Looper, and R. A. Mewaldt (2007), A theoretical model of the inner proton radiation belt, *Space Weather*, *5*, S04003, doi:10.1029/2006SW000275.

Spence, H. E., et al. (2013), Science goals and overview of the Radiation Belt Storm Probes (RBSP) Energetic Particle, Composition, and Thermal Plasma (ECT) suite on Nasa's Van Allen Probes mission, *Space Sci. Rev.*, *179*, 311–336, doi:10.1007/s11214-013-0007-5.

Tu, W., R. Selesnick, X. Li, and M. Looper (2010), Quantification of the precipitation loss of radiation belt electrons observed by SAMPEX, *J. Geophys. Res.*, *115*, A07210, doi:10.1029/2009JA014949.

Zhao, H., and X. Li (2013a), Inward shift of outer radiation belt electrons as a function of *Dst* index and the influence of the solar wind on electron injections into the slot region, *J. Geophys. Res. Space Physics*, *118*, 756–764, doi:10.1029/2012JA018179.

Zhao, H., and X. Li (2013b), Modeling energetic electron penetration into the slot region and inner radiation belt, *J. Geophys. Res. Space Physics*, *118*, 6936–6945, doi:10.1002/2013JA019240.

Zhao, H., X. Li, J. B. Blake, J. F. Fennell, S. G. Claudepierre, D. N. Baker, A. N. Jaynes, D. M. Malaspina, and S. G. Kanekal (2014a), Peculiar pitch angle distribution of relativistic electrons in the inner radiation belt and slot region, *Geophys. Res. Lett.*, *41*, 2250–2257, doi:10.1002/2014GL059725.

Zhao, H., X. Li, J. B. Blake, J. F. Fennell, S. G. Claudepierre, D. N. Baker, A. N. Jaynes, and D. M. Malaspina (2014b), Characteristics of pitch angle distributions of 100s keV electrons in the slot region and inner radiation belt, *J. Geophys. Res. Space Physics*, *119*, 9543–9557, doi:10.1002/2014JA020386.